CEAS Aeronautical Journal
https://doi.org/10.1007/s13272-026-00962-2

ORIGINAL PAPER

Retrieving spectral information of individual noise sources from aircraft flyover array measurements

Irina Besnea[1] · Irene C. Dedoussi[1,2] · Pieter Sijtsma[3] · Mirjam Snellen[1]

Received: 27 August 2025 / Revised: 15 February 2026 / Accepted: 25 March 2026

Abstract

The normalized fan rotational speed per aircraft engine (N1%) is an essential input parameter to noise prediction models, but is often confidential and not directly accessible to researchers. The aircraft acoustic signal characteristics, and specifically the tonal component, can be used to extract this parameter. However, existing methodologies estimate N1% parameters from whole-aircraft spectra, which can lead to inaccurate estimations. This research aims at investigating the various tonal contributions by isolating and reconstructing spectrograms of individual noise sources using acoustic arrays. Using such arrays, it is possible to discriminate between the various components that contribute to the noise emitted by the aircraft, especially between the engines, but also the nose landing gear. From the resulting engine-specific spectrograms the N1% of individual engines for 24 aircraft were obtained. For the A321neo and the B737NG, it is found that, for 80% of the analyzed aircraft, additional engine tones accompany the higher harmonics of the engine blade passage frequency, with these additional tones corresponding to twice the shaft frequency. In addition, it was found that N1% differences between the two engines are reflected in the spectrograms and that a tone stemming from the nose landing gear can be present, resulting in a complex pattern of tones in the whole-aircraft spectrogram. The insights on the various tonal contributions to the received signal are of importance regarding the further development of methods that aim to extract the engine setting from aircraft noise measurements and as such for enabling more accurate noise calculations.

Keywords N1% fan speed estimation · Acoustic array beamforming · Engine tonal harmonics · Source-specific spectrogram reconstruction

1 Introduction

The aviation industry is experiencing a resurgence after two years of COVID-19 slowdown. As the number of aircraft movements increases, there is a corresponding rise in aviation-related emissions, both in terms of noise and chemical emissions. Near airports, these emissions can lead to noise complaints and health concerns for surrounding communities [1].

To predict the effects on the communities, policymakers use models. Regarding noise, these models are predominantly semi-empirical, employing data acquired during controlled experiments, collected around airports or during certification (e.g. ECAC.CEAC's Doc 29 [2], the successor of FAA's INM: AEDT [3], or sonAIR [4]). The models require a variety of inputs, such as the location of the aircraft, aircraft configuration, weather, and the thrust setting or the N1% (normalized fan rotational speed of an aircraft engine). The fan's rotational speed affects the airflow and

Irene C. Dedoussi, Pieter Sijtsma and Mirjam Snellen have contributed equally to this work.

✉ Irina Besnea
i.besnea@tudelft.nl

Irene C. Dedoussi
icd23@cam.ac.uk

Pieter Sijtsma
pieter.sijtsma@psa3.nl

Mirjam Snellen
m.snellen@tudelft.nl

[1] Operations and Environment, Faculty of Aerospace Engineering, Delft University of Technology, Kluyverweg 1, 2629 HS Delft, The Netherlands

[2] Whittle Laboratory, Department of Engineering, University of Cambridge, 1 JJ Thomson Avenue, Cambridge CB3 0DY, UK

[3] PSA3, Kanaaldijk 20, 9493 TE De Punt, The Netherlands

Published online: 10 April 2026

thrust produced by the engine, which, in turn, impacts the generated noise. Thus, noise models use the thrust setting (or the related N1%) to estimate the sound power level emitted by the aircraft, generally taking into account the specific engine type and its associated noise characteristics. The N1% parameter is also relevant for estimating the impacts on the atmosphere, as it is linked to the emissions' quantities of gases and particles from the aircraft engines [5].

Typically, the N1% or thrust values used for predicting the environmental effects of aviation are based on values listed for standardised procedures. However, these resulting estimates for N1% or thrust are known to be rough estimates only (for example, due to the use of simplified thrust profiles and default assumptions in best-practice noise models [6, 7]), with potentially significant deviations from the actual values, negatively affecting the accuracy of the model predictions. Therefore, there is a need to develop methodologies to obtain N1% or thrust estimates that better reflect real-world operational conditions. Several such methodologies have been proposed in the literature. Some of these consider the actual aircraft track and use it to estimate the thrust [8]. Others base the estimates on acoustic measurements per aircraft flyover, either by using the tones corresponding to the blade passage frequency (BPF) or by also accounting for the buzz-saw tones at the shaft frequency (methods as described in [9, 10]). These latter methods are considered of high interest, also given the increasing number of noise monitoring stations. However, to allow for these methods to be put into practice, either for validating the currently used input or to generate the input, more insights into the contributions of the various aircraft noise-generating components to the acoustic measurements are needed. A key limitation of whole-aircraft acoustic approaches is that the measured spectrograms can contain mixed contributions from multiple physical sources (e.g. the left and right engines, airframe components, and landing gear), while engines themselves may operate at different rotational speeds during approach, for instance, due to wind conditions. Although microphone-array beamforming has proven effective for discriminating between aircraft noise source regions [11, 12], it has not been widely used as a pipeline to reconstruct source-specific spectrograms for subsequent determination of the BPF.

In this work, we aim to contribute to the ongoing efforts of deriving accurate estimates for N1% from noise measurements by isolating the acoustic signature per aircraft noise source. We describe a workflow to reconstruct source-specific spectrograms (left engine, right engine, and nose landing gear) from flyover array measurements using conventional frequency-domain beamforming and source-location-based spectral reconstruction. Next, we estimate the BPFs and corresponding N1% values for each engine across 24 operational landing aircraft, enabling identification of engine-to-engine setting differences within the same aircraft. Third, we demonstrate that whole-aircraft spectrograms can be biased by non-engine tones such as a prominent nose landing gear tone in some aircraft types and mixed tonal contributions, motivating source decomposition when extracting engine settings from acoustic data. Finally, we provide a quantitative characterization of secondary tonal components near BPF harmonics, typically consistent with offsets related to shaft frequency (most commonly at twice the shaft frequency for the B737NG and A321neo), and discuss their implications for robust BPF/N1% identification.

In this analysis, the engine setting parameter is expressed as the normalized fan rotational speed N1% of the specific engine model, i.e. $\mathrm{N1\%} = 100n/n_{\max}$, where $n_{\max}$ is the maximum fan rotational speed. The values of $n_{\max}$ are taken from the corresponding engine type certificate data sheets for the engine variants considered (see Table 1). For certain applications, such as noise-power-distance modelling, a corrected fan speed is often used to account for the temperature dependence. However, the required temperature reference is not available in the present dataset. In addition, the objective of this work is to retrieve an engine-setting parameter directly from acoustic observations with minimal auxiliary operational input. Therefore, we adopt N1% as defined in the certification documentation to ensure consistency with operational practice and data availability.

This manuscript is structured as follows: Sect. 2 describes the methods employed to identify and reconstruct the spectrograms of individual contributing noise sources. In Sect.

Table 1 Optimal N1%, BPFs, the absolute difference between engines' N1%, and the multiples of shaft frequencies which explain the additional tones of the measured aircraft

	B737NG	A321neo	E195-E2
Number of aircraft	19	1	4
Number of fan blades	22	20	18
n_{max} at 100%	5175	3281	3461
N1%	52.3–73.8 %	53.7–54%	42.1–51.6%
BPF	993–1402 Hz	588–591 Hz	437–536 Hz
ΔN1% between engines	0–3.6%	0.27%	0.3–3.1%
Multiples of f_{shaft} that explain the additional tones (%)	$2 \cdot f_{\mathrm{shaft}}$ (77% of the 113 sets)	$2 \cdot f_{\mathrm{shaft}}$ (83% of the 6 sets)	No additional tones observed

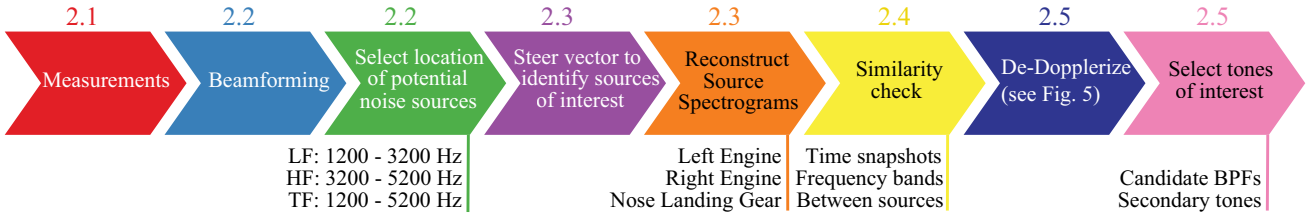

Fig. 1 Workflow of the analysis: each box is described throughout Sect. 2 at the letters above the blocks

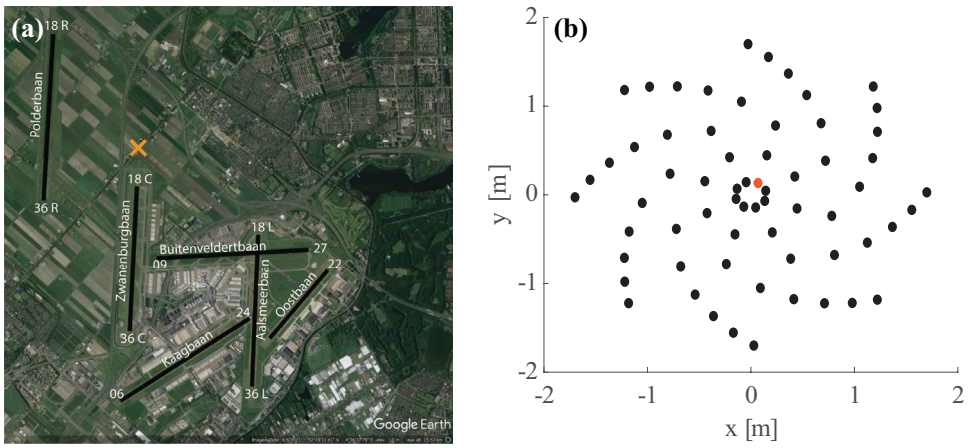

Fig. 2 Experimental set up: **(a)** Measurement location at Amsterdam Airport Schiphol marked with an orange marker. The runways are denoted by the black lines. **(b)** Microphone array configuration (bottom-up view) composed of 64 microphones (mic 2 is marked with orange)

3, we present the results of our analysis. Finally, in Sect. 4, we summarize our findings and discuss their relevance in the context of finding the aircraft engine settings, essential for accurate predictions of the environmental effects of aviation.

2 Methods

This section outlines the methodology used to estimate the rotational speed of the low-pressure spool (N1) of turbofan engines based on acoustic data captured by a 4 m diameter microphone array during aircraft landings. The methodology integrates classical beamforming techniques and pressure spectrogram analysis to process and analyze the acoustic signals.

The following steps, presented in Fig. 1, were undertaken: data acquisition (red block), beamforming over a grid of potential source locations (light blue), source location selection (green) over three frequency bands from the acoustic images obtained from beamforming (denoted with LF, HF, and TF, respectively), use beamforming to focus the array on the identified source locations (purple) to reconstruct the source spectrograms (orange block) of the principal noise sources of interest: the engines and the nose landing gear. Afterwards, a similarity check of the identified sources (yellow block) is performed to check the consistency of identified sources throughout the time snapshots (point 1), over the frequency bands (point 2), and lastly, the correlation between the identified sources, to test if they are generated by the same mechanism (point 3). The next step revolves around the de-Dopplerization of the reconstructed spectrograms (dark blue block). Lastly, the pink block describes the selection of tones of interest, candidate BPFs and the secondary tones.

The detailed procedures and the rationale behind each step are explained in the subsequent sections.

2.1 Measurement campaigns

The measurement campaign took place at Amsterdam Airport Schiphol on the 28th of September 2021. The equipment was set up north of the Zwanenburgbaan (18C) runway at approximately 640 m away from the runway threshold (see Fig. 2a) and consisted of a 4×4 m microphone array with 64 microphones (spatially arranged as in Fig. 2b to allow for acoustic imaging, with a sampling frequency of 50kHz. Spectrograms are computed from 0.05 s blocks (2500 samples at a sampling frequency of 50 kHz) using a Hamming window. The FFT length equals the block length ($N = 2500$), which yields a frequency-bin spacing of $\Delta f = f_s/N = 50000/2500 = 20$ Hz and a Nyquist frequency of 25 kHz. The signal from microphone 2, marked in orange color in the figure, was considered for the spectrograms in the analysis due to its central location and quality. A total of 55 landing aircraft were measured, the majority of which were B737 next-generation (NG) aircraft. This research focuses on three aircraft types, the Boeing

B737NG (19 aircraft), the Embraer E195-E2 (4 aircraft) and the Airbus A321neo (1 aircraft). These account for 24 aircraft analysed in this study, which have been measured while flying above the array at altitudes varying between 34 and 57.5m. The altitudes and other position vector data for this measurement campaign are extracted from Automatic Dependent Surveillance-Broadcast (ADS-B) data collected from the OpenSky database [13].

2.2 Beamforming and source locations

We first visualize the measured pressure signals in the form of spectrograms to assess the frequency content over time. In Fig. 3 we show a representative spectrogram of each analyzed aircraft type, which has been obtained by using the data from a single microphone. A multitude of tones and their harmonics are observed. These are tones that are typically used for estimating the blade passage frequency, where the N1% is determined using the relation $\mathrm{BPF} = \frac{Bn_{\max}\mathrm{N1\%}}{60 \cdot 100}$ with B the number of fan blades and $n_{\max}$ the maximum rotational speed of the fan as defined in the engine certification documents [14–16]. However, these spectrograms do not allow the isolation of the contributions from the various aircraft components to the received signal.

To isolate the sources and understand their contributions to the overall noise, we make use of acoustic imaging techniques. For this research, Conventional Frequency Domain Beamforming (CFDB) [17] was selected due to its robustness. The beamforming output is expressed as:

$$A(f) = \frac{1}{2}\frac{\boldsymbol{g}^* \boldsymbol{P}\boldsymbol{P}^* \boldsymbol{g}}{\|\boldsymbol{g}\|^4} \tag{1}$$

Equation 1 is known as the beamforming equation where the pressure vector $\boldsymbol{P}$ contains the Fourier Transform coefficients at frequency f of the measured acoustic pressure for each microphone (which have not been corrected for Doppler-shift). The steering vector $\boldsymbol{g}$ contains the phase shifts corresponding to the distance between a considered potential source position and each of the array microphones. The asterisk (*) denotes the complex conjugate transpose. After applying Eq. 1 to all potential source locations within a scan grid, a source map is obtained, mapping the beamforming output on the scan grid.

CFDB permits the identification of noise sources per frequency. By summing the beamforming output over a range of frequencies (incoherent summation), the low resolution at low frequencies and the sidelobes at high frequencies are counteracted to some extent. In this research, we have selected three frequency bands for the incoherent summation. We define a Low Frequency (LF) band between 1200 and 3200 Hz, a High Frequency (HF) band between 3200 and 5200 Hz and the Total Frequency (TF) band between 1200 and 5200 Hz. The LF and HF bands have been selected such that either the engines or the airframe sources are expected to be dominant

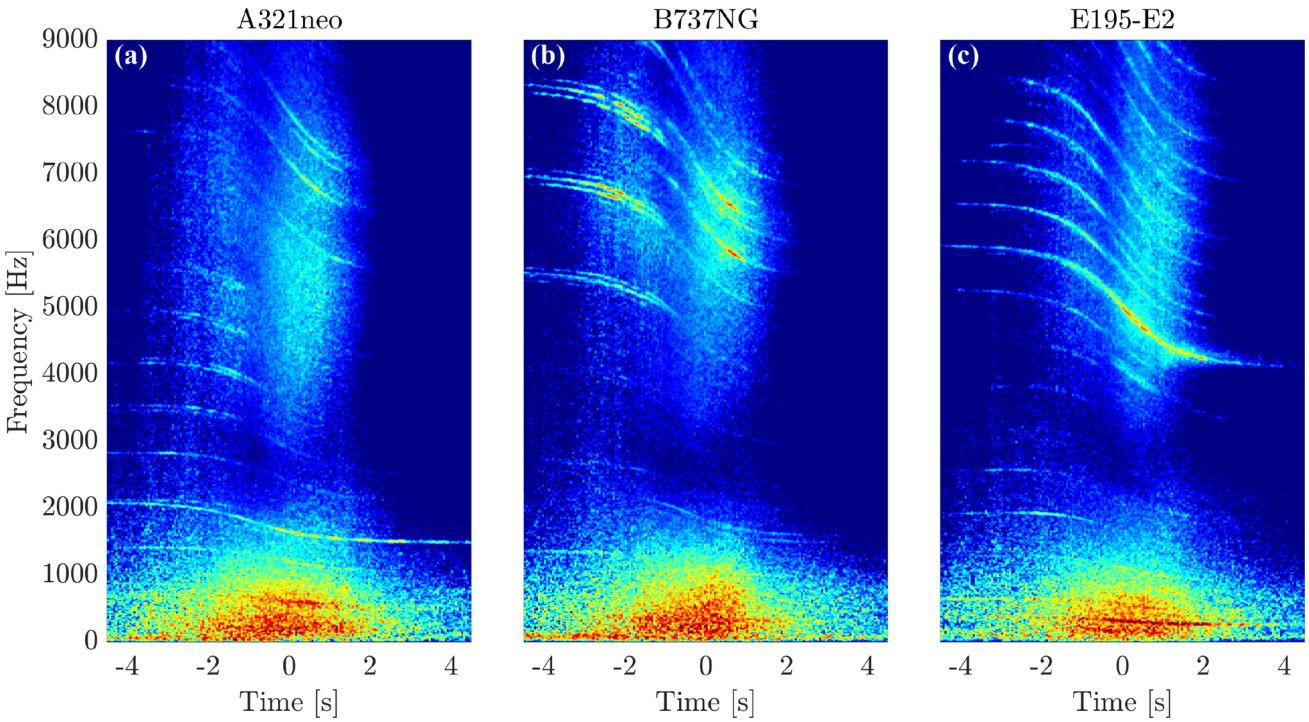

Fig. 3 Representative spectrograms landing of (**a**) A321neo, (**b**) B737NG, and (**c**) E195-E2 acquired during the measurement campaign. These spectrograms are computed using the signal from microphone 2

for landing aircraft [18]. Beamforming has been applied to snapshots lasting 0.05s of data spanning the full aircraft flyover. From the beamforming results the sources have been identified per fly-over and their locations have been determined. Illustratively, Fig. 4 shows how beamforming can be used to identify the noise sources for different aircraft types using a dynamic range of 5 dB. The top part of the figure shows the beamforming outputs for each representative aircraft type in the frequency band 1700–1900 Hz. Note that the identified sources in this band consist mainly of the landing gear for the different aircraft types. In the case of the Embraer E195-E2 (Fig. 4c), the engines (especially the left engine) are also dominant over this frequency band. The bottom part of the figure shows the beamforming output in the frequency band between 4600–4800 Hz. In this case, the engines are the main sources visible in the plots.

2.3 Selection and spectral reconstruction of individual aircraft noise sources

To decompose the aircraft spectrogram into the underlying contributions originating from their individual noise sources, the location of each source is identified on the aircraft CFDB outputs: For each flyover and for each 0.05 s snapshot, dominant source locations are identified from the CFDB maps within each of the three frequency bands. The sequence of identified locations across consecutive snapshots forms a temporal source-location track for each band. As a next step, the steering vector $\boldsymbol{g}$ is pointed to the individual noise source locations, permitting to extract the spectrogram of this source for each snapshot, again for the three bands separately. Thus, in our study, we computed the source noise spectrum for all of the manually selected locations. The concatenation of the individual source spectra over time yields each source's spectrogram. Different frequency bands contain different noise sources as the main noise contributors. For example, we expect the airframe noise (i.e. nose landing gear, main landing gear, flaps/slats, etc.) to be dominant in the lower frequency ranges (1200–3200 Hz), while engine component noise is dominant both in the lower frequencies (jet noise) but also in the higher frequency ranges (3200–5200 Hz) [18]. Consequently, the nose landing gear is, for the majority of the measurements, not visible in the HF beamforming plots and there will thus be no nose landing gear spectrogram derived from the HF results. Various sources can appear also at slightly different locations, for the three frequency bands, on the projected aircraft geometry, due to the imperfectness of the measurements or because of varying (with frequency) directionality of the sources. Although for the similarity check (see Sect. 2.4), we considered all the identified sources, i.e. engines (inlet and exhaust noise), nose and main landing gear, high lift devices, and reflections, the study focuses on the nose landing gear and the engines for the correct estimation of the BPF per engine.

2.4 Similarity analysis

We assess the independence of all identified sources in the CFDB beamforming outputs from the following three perspectives:

1. Consistency of relative locations of identified noise sources across time snapshots: Following the moving-source array-processing approach described by Sijtsma et al. [19], we compute the correlation between CFDB

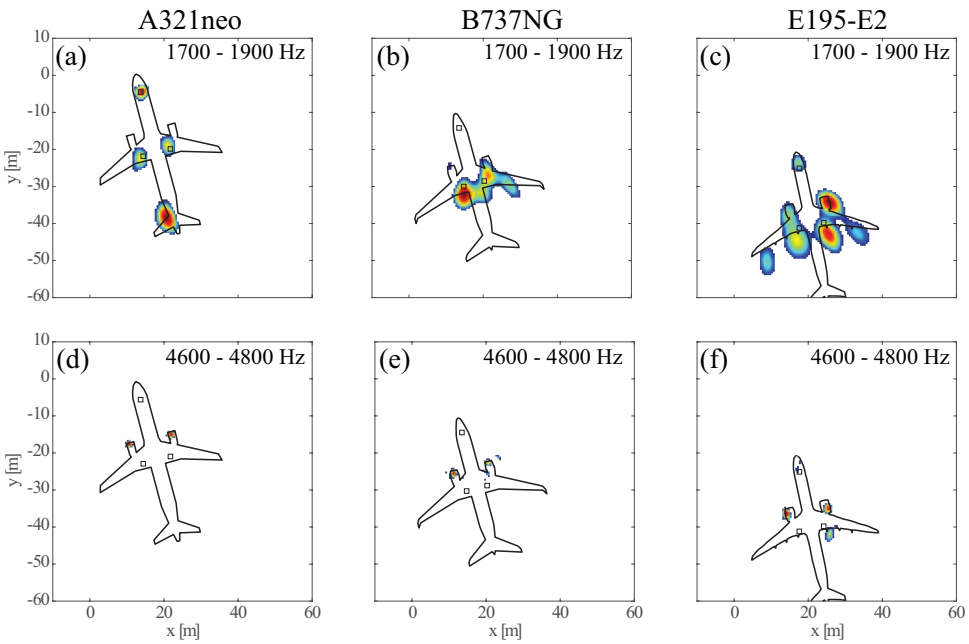

Fig. 4 Aircraft beamforming plots for two frequency bands: 1700–1900 Hz (top: **a**, **b**, **c**) and 4600–4800 Hz (bottom: **d**, **e**, **f**) with superimposed aircraft geometries: **a**, **d** A321neo, **b**, **e** B737NG, and **c**, **f** E195-E2. The selected time snapshot is −0.85s with respect to t = 0s as the overhead position. The landing gear positions are indicated by the squares. The dynamic range of the beamforming plots is 5 dB

source maps of consecutive snapshots to verify that dominant sources persist at consistent relative positions.

2. Similarity in source auto-spectrum for almost co-located sources as identified in the three different frequency bands: We assess the agreement between the full source spectra found for sources appearing roughly, but not exactly, at the same spatial location for the three different frequency bands by computing the correlation coefficient between the full spectra.
3. The match in spectral content between different sources: We test the similarity between all sources using the correlation coefficients between the auto-spectra of the sources over the entire flyover, e.g. between sources located around the nose landing gear and the engines, the main landing gear and the engines, etc.. Low correlation indicates limited relation to the other identified sources. Higher correlations indicate that the spatial resolution is too limited to prevent the estimates of the spectra for one location from having contributions from sources at other locations or that sources actually have a similar origin with one source for example being a reflection of another source. This analysis thus allows us to test the hypothesis of whether the “flaps" (visible in LF) and the “engine reflections" (visible in HF and TF) are the same or not. We consider two identified sources as the same when the correlation coefficient exceeds 0.6.

2.5 De-dopplerization and selection of candidate blade passage frequencies

The objective of this section is to remove the Doppler shift from the reconstructed source spectrograms in order to enable robust identification of tonal components (BPF and harmonics) and subsequent estimation of engine setting parameters. The de-Dopplerization procedure consists of four steps: (i) computing an initial Doppler correction factor from ADS-B geometry, (ii) tracing of a dominant observed tone $f_{obs}(t)$ in the reconstructed spectrogram, (iii) selecting the emitted tone f_0 by RMSE minimization between measured and modeled frequency results, and (iv) applying the resulting Doppler correction to the reconstructed engine spectrograms.

The Doppler frequency shift for a moving source and emitted tone f_0 is described by

$$f_{\text{obs}} = f_0 \left(\frac{1}{1 - M \cos\theta} \right) \tag{2}$$

with f_{obs} the observed frequency, M the Mach number and with the part between brackets often denoted as the Doppler correction factor. The angle $\theta(t)$ is defined by the line-of-sight between source and receiver. For the straight track geometry used here we evaluate $\cos\theta(t)$ from the estimated aircraft motion and range $R(t)$, where $(t = 0)$ denotes the time of closest approach (overhead position).

ADS-B provides aircraft position and ground speed at a 1 s update rate, which is sufficient to obtain a first estimate of the observed frequency f_{obs} for a given emitted tone. Therefore, ADS-B remains the primary source for aircraft position and range $R(t)$. However, because the beamforming and spectrogram reconstruction operate on 0.05 s snapshots, we additionally estimate velocity from the displacement of tracked source locations between consecutive snapshots (see the similarity analysis item (1) in Section 2.4). This provides a temporally smoother velocity estimate at the acoustic processing rate, which facilitates fine-tuning of the Doppler correction (see f_{obs} curve in Fig. 5a).

Because the recordings are taken during the final portion of the approach, close to touchdown and under low and steady wind conditions, we assume that engine setting variations within the analysed interval are limited.

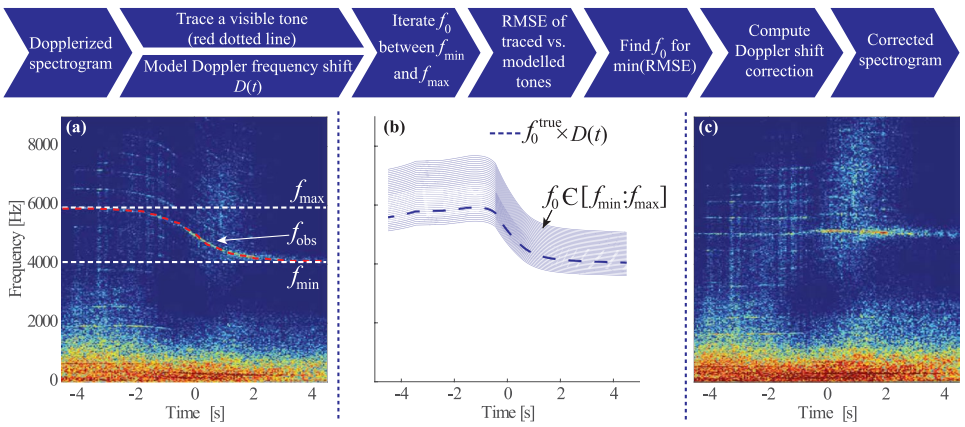

Fig. 5 Description of the de-Dopplerization approach. **(a)** The spectrogram of the right engine of a landing E195-E2 with the observed tone (f_{obs}) (red dotted line) and the minimum and maximum frequency bounds (white dotted lines). **(b)** The reconstructed Dopplerized tones iterating f_0 between the bounds and multiplying it with $D(t)$ (blue lines) with the closest tone to f_{obs} in dashed blue line. **(c)** The de-Dopplerized spectrogram using the optimal f_0 as found in the middle plot

This reduces short-term N1 fluctuations and supports the use of a single emitted tone (f_0) when comparing the frequency variations observed in the measured spectrogram with those determined by the above equation. It is expected that the maximum Doppler shifted frequency occurs at time instances with the aircraft far away and approaching the array, whereas the minimum frequency observed corresponds to the aircraft flying away from the array. By considering a number of potential values for the emitted frequency of the tone, f_0, between the minimum and maximum and comparing the corresponding expected Doppler-shifted frequencies with the traced tone of step (ii), an estimate for f_0 is obtained by selecting the value that minimizes the RMSE (root-mean-square error) between the traced tone and the modelled Doppler-shifted tone (f_0^{true} in Fig. 5b). The resulting Doppler correction factor (denoted as $\mathrm{D}(t)$ in Fig. 5b) is used for the final de-Dopplerization of the spectrogram. The result for a representative measurement is shown in Fig. 5c.

As the next step, i.e. to determine the BPF, but also to identify all other tones in the signal, we select the time snapshot where tonal components are most prominent (highest tonal contrast) for each de-Dopplerized spectrogram. We average the spectra around this time snapshot over a range of ± 0.5 s. The spectrogram and the averaged spectra are shown in Fig. 6a for the Airbus A321neo, Fig. 6b for one of the Boeings B737NG and in Fig. 6c for one of the Embraers 195-E2. Note the double peaks observed in the cases of the A321neo and the B737NG.

Using the peaks (indicated by the dots in the averaged spectra) an iterative procedure is applied to determine when peaks are actually multiples of each other. Since we consider spectrograms that correspond to a single engine only, we do not expect multiple BPFs per engine to be present. Indeed this is confirmed by the analysis since the tones in the spectrogram are found to be related to 1 BPF, but often accompanied by tones around it related to the shaft frequency. The agreement between the determined BPF and the corresponding harmonics (thus multiples of the BPF) with those actually identified in the spectra is quantified by the root-mean-square error (RMSE) between these two sets of tones.

With the thus found BPF, the corresponding shaft frequency f_{shaft} is computed via

$$f_{\text{shaft}} = \frac{\text{BPF}}{B} \tag{3}$$

where BPF is the determined blade passage frequency and B is the number of fan blades.

3 Results

3.1 Spectrograms per aircraft source

The approach presented in the previous section permits us to reconstruct the spectrograms of individual sources and compute their individual characteristics (Examples of these were already shown in the previous section for the right engine). Figure 7 shows the spectrograms corresponding to the Airbus A321neo individual engines and the nose landing gear in addition to the total spectrogram of the measurement. The spectrogram amplitudes have been corrected for the aircraft's distance to the microphone array. Both the nose landing gear and each engine display different characteristics which would have been challenging to isolate from the whole-aircraft spectrogram.

The nose landing gear of the A321neo is easily identifiable and isolated from the engines. It displays a specific tone varying between 1500 and 2000 Hz due to the Doppler

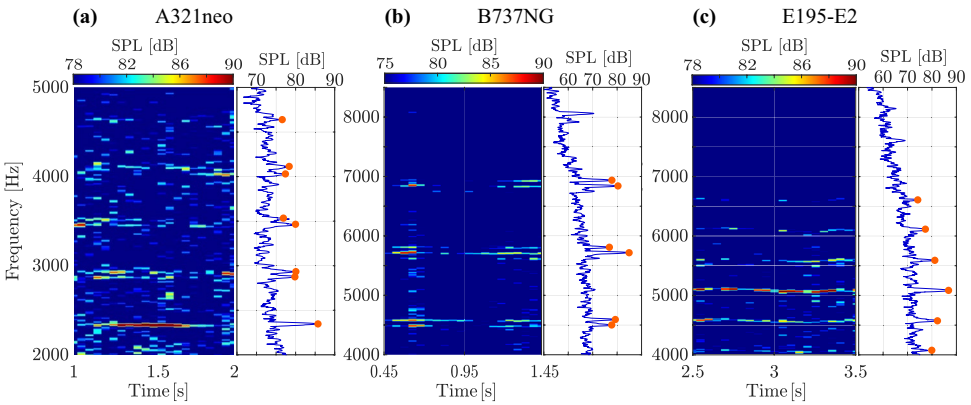

Fig. 6 Selecting the peaks (candidate BPF harmonics) for the right engines of (**a**) Airbus A321neo, (**b**) Boeing B737NG, (**c**) Embraer E195-E2. For each aircraft type, the spectrogram over the selected 1-second time snapshot is presented on the left side. The right side shows the average spectra over the time snapshot, and the selected peaks are marked with orange dots

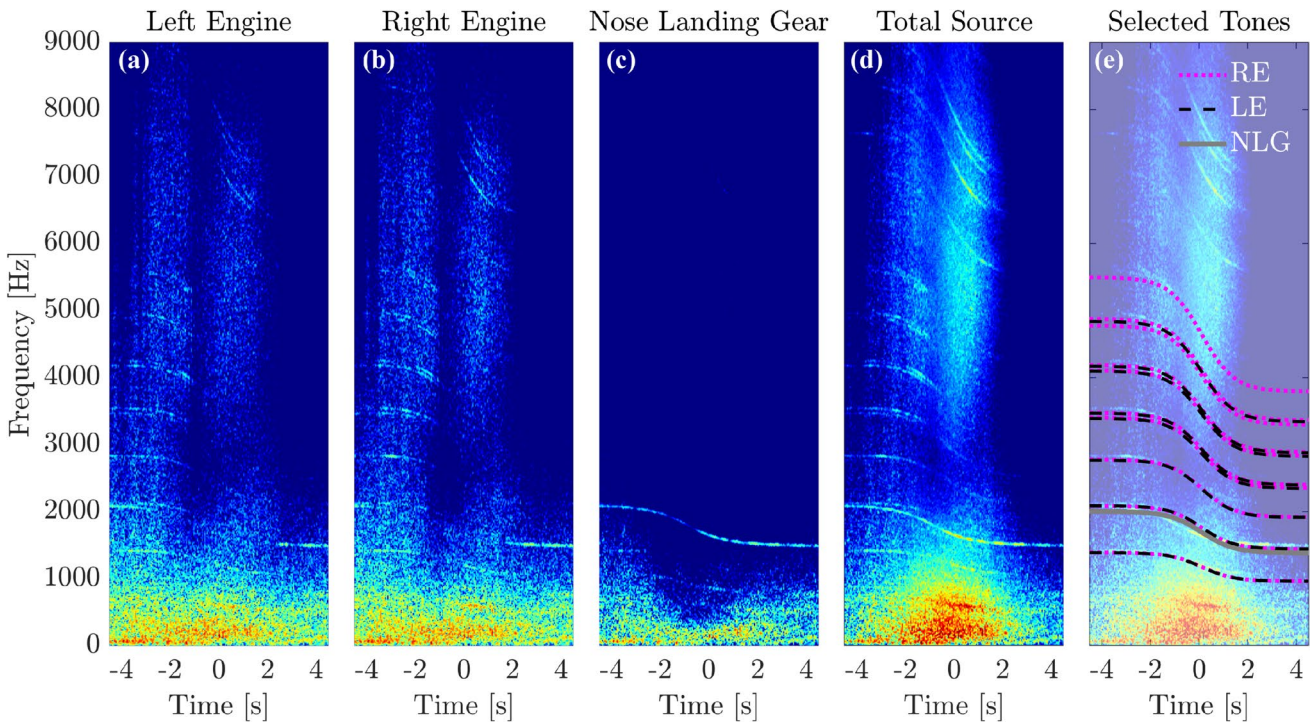

Fig. 7 A321neo reconstructed spectrograms of (**a**) left engine (LE), (**b**) right engine (RE), (**c**) nose landing gear (NLG), (**d**) total spectrogram, and (**e**) total spectrogram with superimposed tonal contributions of each source

Effect. This has been observed before [9, 20, 21], and likely occurs due to a cavity present on the landing gear. After de-Dopplerization, we determined that the landing gear tone occurs at 1730 Hz which is in agreement with the previous observations and corresponds to a half-wavelength of approximately 10 cm [20, 21]. Many components of the nose landing gear mechanism have comparable sizes, i.e. the width of a towing fitting, which could explain this tone [20, 21]. In the case of the B737NG (see Fig. 11) and the E195-E2 (Fig. 7) shown in the Appendix, there is no prominent nose landing gear tone visible.

The individual engine spectrograms of Fig. 7 show that the tones per engine are now distinguishable. There is a slight shift in BPF between the engines as the right engine exhibits slightly higher tones than the left engine (see Fig. 7e). This shift is due to slightly different rotational speeds between the fans of the left versus right engines of the aircraft, probably applied to correct for the wind direction. We also notice in the case of the A321neo and the B737NG that each BPF harmonic is accompanied by an additional tone. This is not present in the case of the E195-E2 (Fig. 12) in Appendix Appendix A. The presence of such tones can hinder the correct determination of the BPF and its corresponding N1% (see Sect. 2.5) if not properly accounted for. For one representative B737NG, Fig. 8 shows the shifts between the two engine tones as well as the contribution to the total spectrogram. The offset between the engines' BPF harmonics as well as the additional tones accompanying them can be observed in the exemplary frequency band of 7000–9000 Hz. In the total spectrogram, we can identify the harmonics of each engine. It can be observed that the left engine is exhibiting higher tones than the right engine tones.

3.2 Source identification

Despite the fact that sources show up at different locations, they still might be related, e.g. one source actually being a scattered version of another source. Therefore, the similarity between the sources identified in the beamforming outputs is checked from three different points of view as described in Sect. 2.4, i.e. between time snapshots, between frequency bands, and between identified sources. The time perspective (Sect. 2.4, point 1) was already used to estimate the velocity of the aircraft, and indicated high similarity between beamforming outputs for subsequent time snapshots (see Figs. 13 and 14 for representative examples) and thus the persistent relative location of the sources visible in the acoustic images. This section presents the results from evaluating the correlation coefficient between spectra determined for almost (but not exactly) co-located sources for the

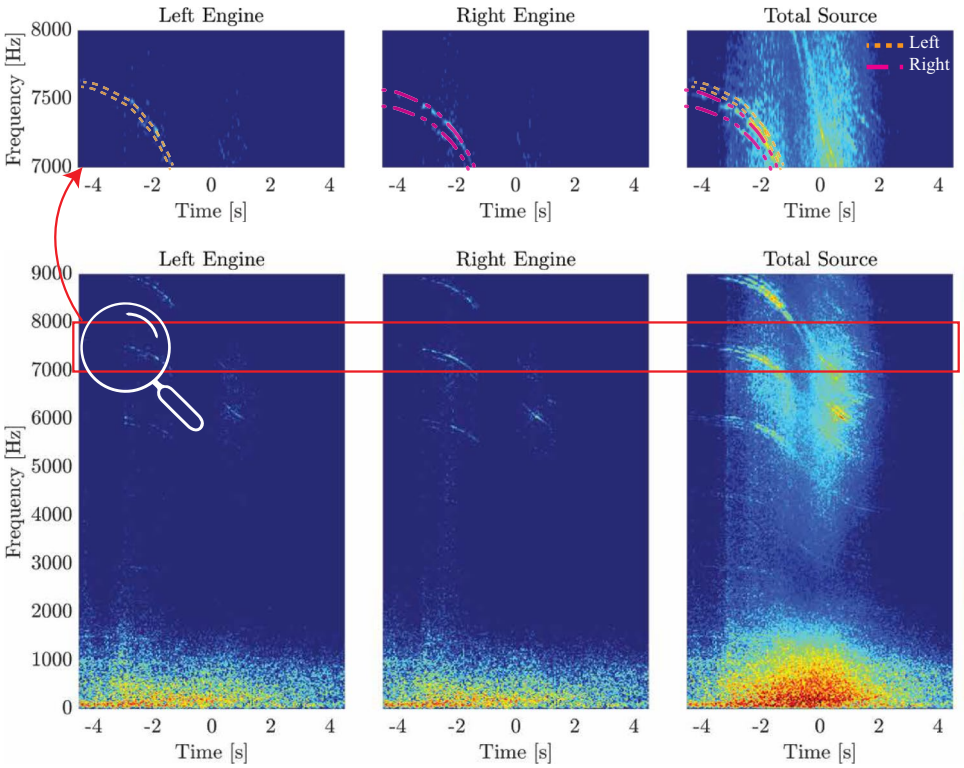

Fig. 8 B737NG reconstructed spectrograms of the left engine, right engine and total spectrogram on the bottom side. The red boxes mark the frequency region of interest (7000–8000 Hz) which is shown magnified in the upper figures. The tones identified in each plot of the engines are marked with dashed colored lines (left: orange, right: magenta). This figure is part of Fig. 11, but zoomed in on the frequency range of 7000–8000 Hz

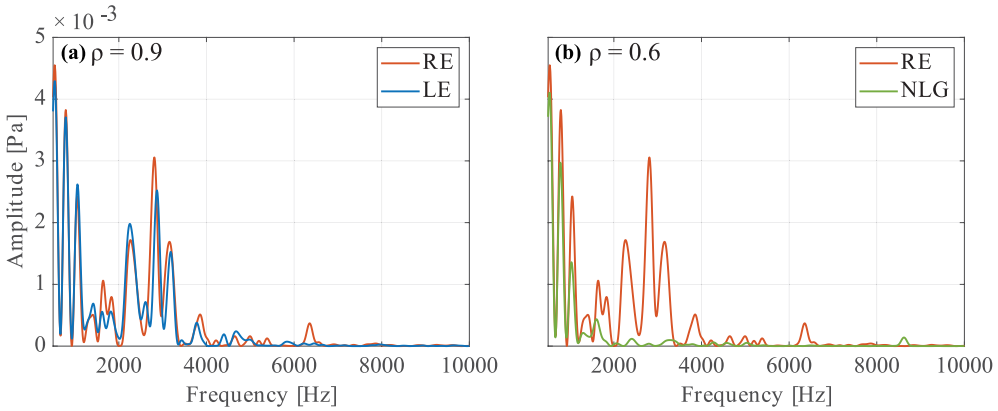

Fig. 9 **(a)** Exemplary spectra (from 500 to 10000 Hz) of the right engine and left engine of the A321neo. Their similar shapes yield a correlation coefficient of 0.9. **(b)** Exemplary spectra (from 500 to 10000 Hz) of two dissimilar sources with a low correlation of 0.6 (right engine and nose landing gear of the A321neo)

different frequency bands and between different identified sources, respectively. Regarding the first (Sect. 2.4, point 2), the results were found to be consistent for each of the sources over the three bands, e.g. correlation coefficients and confidence interval for all engines were 0.99 (68% confidence interval [0.92 1]).

From the perspective of testing between sources (Sect. 2.4, point 3), the identified “flaps" and “engine reflections" on both the right and the left side of the aircraft are highly correlated (0.99) indicating that they are indeed occurring due to reflections or scattering of the engine noise (correlation coefficients between 0.86 and 0.9 with each engine). Consequently, it cannot be stated with certainty that the noise contribution of the flaps can be quantified from this analysis. A similar conclusion applies to the left and right main landing gear, the derived spectra of which are also highly correlated to that of the engines. In contrast, the contribution of the nose landing gear is distinguishable from the remaining identified sources

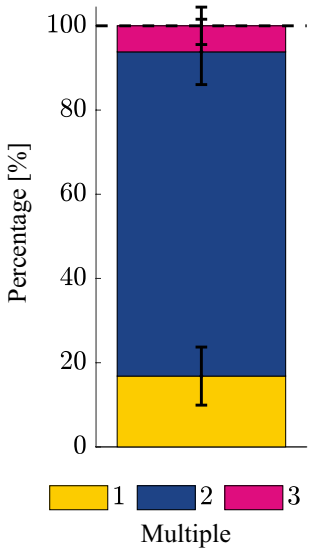

Fig. 10 Multiples of f_{shaft} that can explain the frequency offsets within the 119 identified sets (pairs) of tones

as shown by its lower correlation coefficient of 0.6 with the engines. Figure 9 shows the comparison between the spectra of highly correlated sources (the left and right engines) versus the spectra of weakly correlated sources (in this case the right engine with the nose landing gear). It should be noted that the frequencies below 1000 Hz are not used for the source identification where only frequencies above 1200 Hz are used. The high correspondence between the spectra for frequencies below 1000 Hz is due to the limited spatial resolution of the array for these low frequencies. Consequently, the spectra below 1000 Hz are, for all scan points in the grid, contaminated by contributions from the most dominant source in this frequency range, in this case, the engines.

3.3 Offset between BPFs' harmonics and the additional tones

In the individual-source spectrograms of the B737NG and A321neo, the harmonics of the blade passage frequency (BPF) are frequently accompanied by a secondary set of tones located close to the BPF harmonics and primarily observable in spectrum above 4kHz (see Fig. 6). These secondary tones can be described as occurring at approximately $n \cdot \text{BPF} \pm \Delta f'$, where n is the harmonic index and $\Delta f'$ is most commonly consistent with approximately $2 f_{\text{shaft}}$ for the analysed cases.

A plausible explanation for these secondary tonal components at approach power is the interaction between multiple rotating components on the low-pressure spool, such as fan and booster (low-pressure compressor) stages, which generate additional discrete spectral components and interaction tones close to fan-related harmonics. Such fan-booster interaction tones have been documented in ducted-fan measurements, where the presence of multiple rotating sources leads to additional tonal content beyond the primary BPF harmonics [22, 23].

Figure 10 shows multiples of f_{shaft} (for our measurement ranging between 1 and 3 times f_{shaft}) that can explain the frequency offsets within the identified sets (pairs) of tones and their 95% binomial proportion confidence interval over the sample. Approximately 80% of the offsets between the BPF harmonics and their additional tone relate to twice the shaft frequency, f_{shaft}.

3.4 N1% Estimation

The conversion from BPF to N1% uses the blade count B and $n_{\max}$ for the engine models listed for each aircraft in Fig. 1. Thus, the N1% is computed directly from the BPF (see Sect. 2.2). For all analysed B737NG, the found BPFs of the right engines ranged between 993 znd 1402 Hz, corresponding to values of N1% between 52.3 and 73.8%. For the left engines, the BPFs ranged between 1046 and 1402 Hz equivalent to N1% values between 55.1% and 73.8% (Table 1). The BPFs were determined with RMSE of 6.3–115.8 Hz for the right engines and 1.8–17.6 Hz for the left engines, respectively (Table 2). The N1% of the engines and the N1% differences between the engines fall within ranges as expected for approach procedures [24].

4 Conclusion

Isolating the individual noise contributions of the aircraft noise sources facilitates the accurate determination of the N1% value of each engine, a crucial input parameter in both aircraft noise and emissions prediction models. We demonstrate the various tonal contributions that should be taken into account when extracting N1% using solely acoustic measurements, through aircraft noise source decomposition. With the use of beamforming techniques, we show that it is possible to isolate individual sources and reconstruct their spectrograms. This approach constitutes a reliable method to extract detailed observations about aircraft noise components, e.g. engine and NLG tones, as well as additional BPF harmonic tones.

The correlation analysis in this study tested the independence of several identified sources, i.e. whether they are likely to be due to scattering of the sound of a strong noise source such as the aircraft engine, the result of limited spatial resolution of the array or whether they are really different individual sources. In the case of the A321neo, where the nose landing gear is very prominent, we could, demonstrated by an average low correlation coefficient of ≈ 0.6, distinguish between the engines and the nose landing gear as individual noise sources.

By considering the noise from the engines, we observed that for some aircraft types, mainly B737NG, each engine blade passage frequency and their harmonics are accompanied by an additional set of tones which should be taken into account for an accurate N1% extraction. We attribute this phenomenon to the modes of the shaft rotational frequency, based on the outcomes of our analysis. This phenomenon is observed for operational aircraft and we conclude that, for both the A321neo and B737NG, these additional tones correspond to twice the mode of the shaft frequency with an incidence of approximately 80% throughout the sample.

Our methodology advances our understanding of the individual aircraft noise sources during the final approach stage of landings. The results emphasize the necessity of addressing engine spectra individually to support precise N1% estimation (RMSE of maximum approximately 18 Hz, see Table 2). The offset in BPFs between the engines of the same aircraft can range up to 69 Hz, with a corresponding ΔN1% difference of 3.64% between engines.

Expanding the method to different trajectory segments would require acoustic measurements from arrays of bigger apertures compared to the 4 m diameter array from this study. The bigger aperture would increase the resolution and discrimination of aircraft noise sources at greater distances/altitudes (as expected throughout the flight legs preceding the final approach).

These results support more reliable extraction of engine-setting parameters from acoustic measurements by showing when whole-aircraft spectrograms can be confounded by source mixing, such as either landing gear tones or secondary engine tones, and by enabling per-engine estimation of BPF and N1%. This directly benefits applications that rely on realistic operational engine settings as inputs, including improved noise prediction and calibration efforts that go beyond default thrust-profile assumptions [25].

Overall, the presented approach and results provide an essential step in improving aircraft information extraction analyses from acoustic measurements and contribute to a better characterization of the real-world footprint of in-operation aircraft. We anticipate that the findings of this research are very valuable to the scientific community as an essential step in steering future aircraft information extraction analyses from acoustic measurements.

Appendix

Source and total spectrograms of B737NG and E195-E2

This appendix contains the reconstructed and total spectrograms of both a B737NG and an E195-E2 as shown for the A321neo in Fig. 7.

See Figs. 11 and 12.

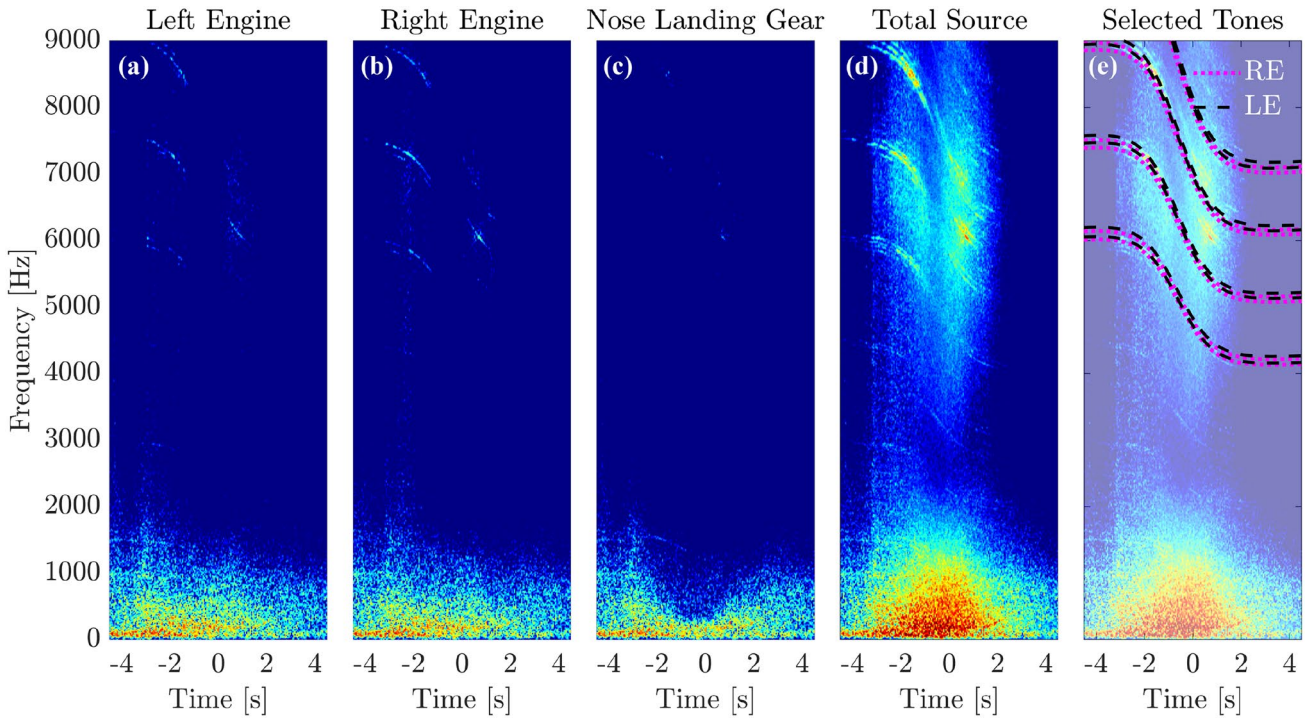

Fig. 11 B737NG reconstructed spectrograms of (**a**) left engine (LE), (**b**) right engine (RE), (**c**) nose landing gear (NLG), (**d**) total spectrogram, and (**e**) total spectrogram with superimposed tonal contributions of each source

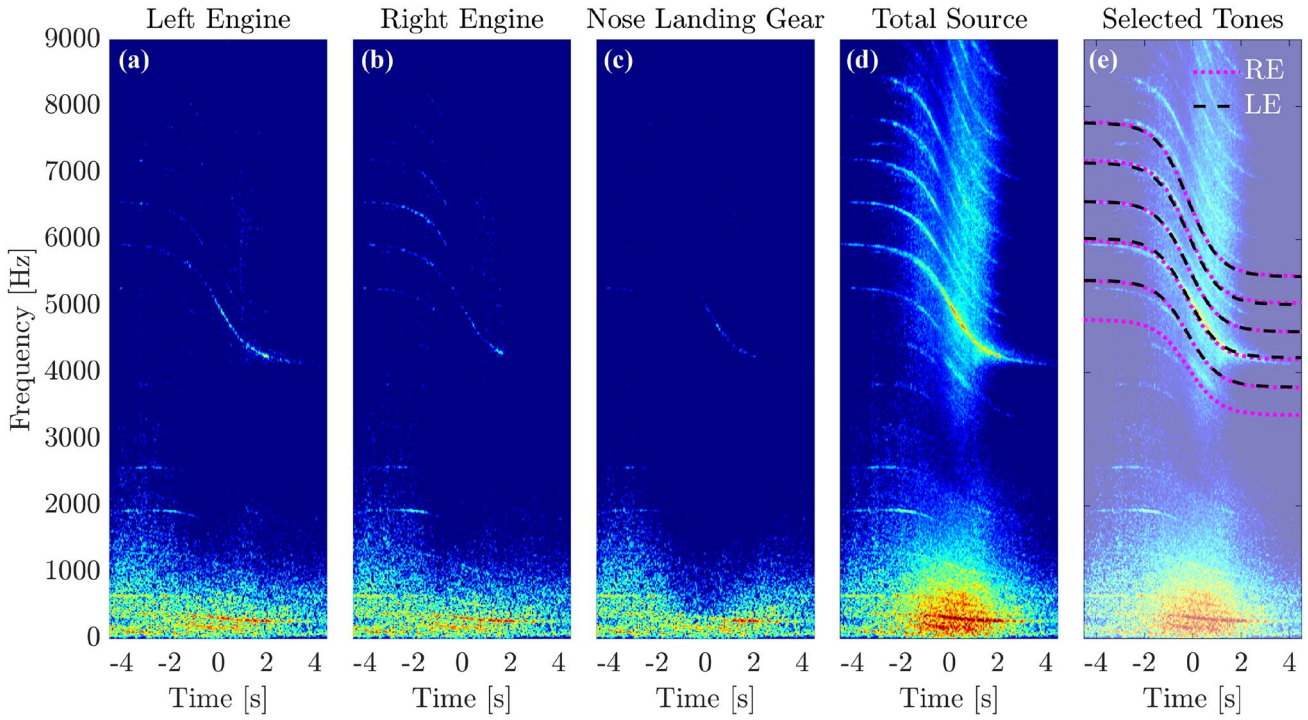

Fig. 12 E195-E2 reconstructed spectrograms of (**a**) left engine (LE), (**b**) right engine (RE), (**c**) nose landing gear (NLG), (**d**) total spectrogram, and (**e**) total spectrogram with superimposed tonal contributions of each source

Table of BPF and N1% values

This appendix presents the estimated BPF (and associated N1%) values of the entire measurement set and their root mean squared error. The values are presented for each engine. The table also offers information over the specific aircraft type and engine type.

See Table 2.

Snapshot-to-snapshot consistency checks (spectra and CFDB maps)

This appendix provides representative examples supporting the snapshot-to-snapshot consistency assumptions used in the analysis. Figure 13 shows a representative CFDB example of consecutive snapshots from an E195-E2 flyover, illustrating that the dominant source region remains spatially consistent over time.

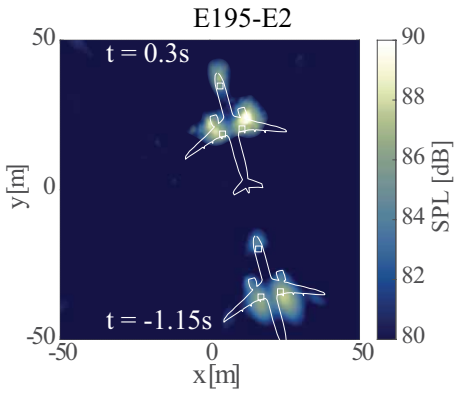

Fig. 13 CFDB map for consecutive snapshots of an E195-E2 flyover (representative example), illustrating that the dominant source region remains spatially consistent across snapshots

Figure 14 shows exemplary spectra of A321neo right engine across 181 snapshots after frequency-shift alignment. Each spectrum is shifted for maximum alignment to the same location (centroid-based alignment within ± 300 bins), compensating for the Doppler-induced shift.

Table 2 Representative aircraft types and engines models considered in this analysis, their altitude at the overhead position above the array, wind conditions and temperature during the measurement campaign, and the estimated optimal N1%, corresponding BPF values in Hz, and their RMSE in Hz

No	Aircraft type	Engine type	Alt (m)	Wind (m/s) (Dir (°))	Temp (C°)	N_{1RE} (%)	BPF_{RE} (HZ)	$RMSE_{RE}$ (HZ)	N_{1LE} (%)	BPF_{LE} (HZ)	$RMSE_{LE}$ (HZ)
1	A321-271NX	2 × PW PW1133G	41	6 (180°)	18.5	53.76	588	4.79	54.04	591	6.01
2	B737-7K2 (WL)	2 × CFMI CFM56-7B22	36	6 (180°)	18.5	59.50	1129	9.25	61.24	1162	10.56
3	B737-8K2 (WL)	2 × CFMI CFM56-7B24	39	6 (180°)	18.5	58.18	1104	9.06	59.60	1131	13.40
4	B737-9K2 (WL)	2 × CFMI CFM56-7B26	57.5	6 (180°)	18.5	61.71	1171	12.16	61.98	1176	12.12
5	B737-8K2 SH	2 × CFMI CFM56-7B26E	57.5	6 (180°)	18.5				62.40	1184	14.55
6	B737-8K2 (WL)	2 × CFMI CFM56-7B24	51.5	6 (180°)	18.5	62.82	1192	15.35	63.08	1197	10.76
7	B737-8K2 (WL)	2 × CFMI CFM56-7BE	34	6 (180°)	18.5	59.66	1132	9.14	60.08	1140	4.11
8	B737-700 (WL)	2 × CFMI CFM56-7B22	47	6 (180°)	18.5	53.23	1010	14.05	55.13	1046	10.76
9	B737-7K2 (WL)	2 × CFMI CFM56-7B22	54	6 (180°)	18.5	62.19	1180	9.06	61.77	1172	10.30
10	B737-8K2 (WL)	2 × CFMI CFM56-7B24	47	6 (180°)	18.5	62.98	1195	11.48	66.61	1264	17.68
11	B737-7K2 (WL)	2 × CFMI CFM56-7B24	49	6 (180°)	18.5	60.55	1149	15.62	60.82	1154	12.53
12	B737-8K2 (WL)	2 × CFMI CFM56-7B2	41.5	6 (190°)	18.6	56.02	1063	10.59	56.28	1068	12.44
13	B737-8BK (WL)	2 × CFMI CFM56-7B24	47	6 (190°)	18.6	64.14	1217	10.57	64.24	1219	13.35
14	B737-7K2 (WL)	2 × CFMI CFM56-7B22	56	5 (170°)	17.4	52.33	993	11.90			
15	B737-8K2 SH	2 × CFMI CFM56-7B27E	48	5 (170°)	17.4	63.03	1196	8.39	62.87	1193	14.53
16	B737-8K2 (WL)	2 × CFMI CFM56-7B26E	57	5 (170°)	17.4	67.51	1281	6.31	64.45	1223	10.08
17	B737-8K2 (WL)	2 × CFMI CFM56-7B24	52.5	5 (170°)	17.4	60.13	1141	11.88	58.39	1108	13.96
18	B737-8F2 (WL)	2 × CFMI CFM56-7B26	48	5 (170°)	17.4	73.89	1402	10.63	73.89	1402	7.99
19	B737-8K2 (WL)	2 × CFMI CFM56-7B24	45	5 (170°)	17.4	63.98	1214	15.87	62.87	1193	1.76
20	B737-7K2 (WL)	2 × CFMI CFM56-7B22E	53.5	5 (170°)	17.4	59.24	1124	8.86	58.66	1113	12.68
21	E195-E2	2 × PW PW1900G Series	54	4 (140°)	14.3	51.33	533	7.32	51.62	536	3.63
22	E195-E2	2 × PW PW1900G Series	52	4 (140°)	14.3	48.73	506	4.15	49.41	513	5.01
23	E195-E2	2 × PW PW1900G Series	54	4 (140°)	14.3	45.75	475	5.38	46.52	483	5.88
24	E195-E2	2 × PW PW1900G Series	56	4 (140°)	14.3	45.27	470	5.53	42.09	437	6.03

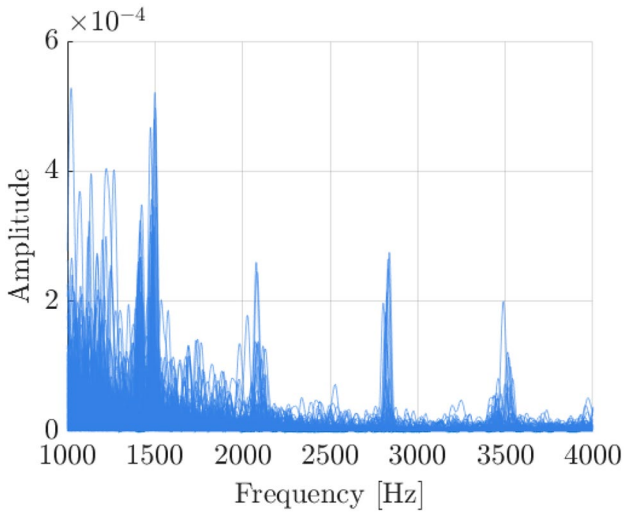

Fig. 14 Aligned A321neo right engine spectra over 181 snapshots to check consistency over the spatial location between consecutive beamforming snapshots

Author contributions I.B. wrote prepared figures and wrote the main manuscript text. I.D. edited parts of section 2. M.S. edited parts of section 3. P.S. edited parts of sections 2.2, 2.3, and 2.4. All authors contributed with research and reviewed the manuscript.

Data availability No datasets were generated or analysed during the current study.

Declarations

Conflict of interest The authors declare no conflict of interest.

References

1. Basner, M., McGuire, S.: WHO environmental noise guidelines for the European region: a systematic review on environmental

noise and effects on sleep. Int. J. Environ. Res. Public Health **15**(3), 519 (2018). https://doi.org/10.3390/ijerph15030519
2. European Civil Aviation Conference: ECAC . CEAC Doc 29 3rd Edition Report on Standard Method of Computing Noise Contours around Civil Airports **1 and 2**(December) (2005)
3. Torija, A.J., Self, R.H., Flindell, I.H.: A model for the rapid assessment of the impact of aviation noise near airports. J. Acoust. Soc. Am. **141**(2), 981–995 (2017). https://doi.org/10.1121/1.4976053
4. Wunderli, J.M., Zellmann, C., Köpfli, M., Schwab, O., Schlatter, F., Schäffer, B.: The sonAIR aircraft noise simulation tool. In: INTER-NOISE 2017—46th international congress and exposition on noise control engineering: taming noise and moving quiet (2017)
5. Quadros, F.D.A., Snellen, M., Sun, J., Dedoussi, I.C.: Global Civil aviation emissions estimates for 2017–2020 using ADS-B Data. J. Aircr. **59**(6), 1394–1405 (2022). https://doi.org/10.2514/1.C036763
6. Merino-Martínez, R., Heblij, S.J., Bergmans, D.H.T., Snellen, M., Simons, D.G.: Improving aircraft noise predictions considering fan rotational speed. J. Aircr. **56**(1), 284–294 (2019). https://doi.org/10.2514/1.C034849
7. Merino-Martinez, R., Snellen, M., Simons, D.G.: Calculation of the fan rotational speed based on flyover recordings for improving aircraft noise prediction models. In: Universitätsbibliothek der RWTH Aachen. 1600–1607 (2019) https://doi.org/10.18154/RWTH-CONV-239171
8. Schwab, O., Zellmann, C.: Estimation of flight-phase-specific jet aircraft parameters for noise simulations. J. Aircr. **57**(6), 1111–1120 (2020). https://doi.org/10.2514/1.C035779
9. Snellen, M., Merino-Martínez, R., Simons, D.G.: Assessment of noise variability of landing aircraft using phased microphone array. J. Aircr. **54**(6), 2173–2183 (2017). https://doi.org/10.2514/1.C033950
10. Ramseier, T., Pieren, R.: Estimation of the fan rotational speed using flyover audio recordings. J. Aircr. (2023). https://doi.org/10.2514/1.C037371
11. Sijtsma, P., Stoker, R.: Determination of absolute contributions of aircraft noise components using fly-over array measurements. In: 10th AIAA/CEAS Aeroacoustics Conference. American Institute of Aeronautics and Astronautics, Reston, Virigina (2004). https://doi.org/10.2514/6.2004-2958
12. Ikuta, Y., Imamura, T., Takaishi, T., Kobayashi, T.: Noise prediction for aircraft during approach by neural network using sound source data obtained from microphone array measurement. In: AIAA AVIATION 2023 Forum, pp. 3–20. American Institute of Aeronautics and Astronautics, Reston, Virginia (2023). https://doi.org/10.2514/6.2023-3927
13. Schafer, M., Strohmeier, M., Lenders, V., Martinovic, I., Wilhelm, M.: Bringing up OpenSky: A large-scale ADS-B sensor network for research. In: IPSN-14 Proceedings of the 13th international symposium on information processing in sensor networks, pp. 83–94. IEEE (2014). https://doi.org/10.1109/IPSN.2014.6846743
14. EASA: CFM International CFM56-7B series engines Issue: 07 TYPE-certificate data sheet. technical report january, Department of Transportation Federal Aviation Administration (2023). https://www.easa.europa.eu/en/downloads/7795/en
15. EASA: International Aero Engines PW1100G-JM series engines Issue: 08 TYPE-CERTIFICATE DATA SHEET. Technical Report October, Department of Transportation Federal Aviation Administration (2022). https://www.easa.europa.eu/en/downloads/20016/en
16. EASA: International Aero Engines PW1500G series engines Issue: 09 TYPE-CERTIFICATE DATA SHEET. Technical report, Department of Transportation Federal Aviation Administration (2022). https://www.easa.europa.eu/en/downloads/20863/en
17. Sijtsma, P.: Experimental techniques for identification and characterisation of noise sources. Advances in Aeroacoustics and Applications, VKI Lecture Series (2004)
18. Simons, D.G., Snellen, M., Merino-Martinez, R., Malgoezar, A.M.N.: Noise breakdown of landing aircraft using a microphone array and an airframe noise model. In: INTER-NOISE 2017 - 46th International Congress and Exposition on Noise Control Engineering: Taming Noise and Moving Quiet **2017** (2017)
19. Sijtsma, P.: Identification of noise sources on civil aircraft in approach using a microphone array. Technical report, National Aerospace Laboratory NLR (2005)
20. Merino-Martinez, R., Bertsch, L., Simons, D.G., Snellen, M.: Analysis of landing gear noise during approach. In: 22nd AIAA/CEAS Aeroacoustics Conference. American Institute of Aeronautics and Astronautics, Reston, Virginia (2016). https://doi.org/10.2514/6.2016-2769
21. Merino-Martinez, R., Snellen, M.: Implementation of tonal cavity noise estimations in landing gear noise prediction models. In: AIAA AVIATION 2020 FORUM. American Institute of Aeronautics and Astronautics, Reston, Virginia (2020). https://doi.org/10.2514/6.2020-2578
22. Yu, J., Nesbitt, E., Kwan, H.-w., Uellenberg, S., Chien, E., Premo, J., Ruiz, M., Czech, M.: Quiet Technology Demonstrator 2 Intake Liner Design and Validation. In: 12th AIAA/CEAS Aeroacoustics Conference (27th AIAA Aeroacoustics Conference), pp. 8–10. American Institute of Aeronautics and Astronautics, Reston, Virigina (2006). https://doi.org/10.2514/6.2006-2458
23. Nesbitt, E., Clark, I., Guo, Y., Thomas, R.H.: Flight Effects on Turbofan Fan Tones. In: 30th AIAA/CEAS Aeroacoustics Conference (2024). American Institute of Aeronautics and Astronautics, Reston, Virginia (2024). https://doi.org/10.2514/6.2024-3222
24. Schwab, O., Zellmann, C.: Estimation of flight-phase-specific jet aircraft parameters for noise simulations. J. Aircr. **57**(6), 1111–1120 (2020). https://doi.org/10.2514/1.C035779
25. Grift, R., Snellen, M., Amiri-Simkooei, A.: Aircraft noise model improvement by calibration of noise-power-distance values using acoustic measurements. CEAS Aeronaut. J. (2025). https://doi.org/10.1007/s13272-025-00902-6